Smith, A. & Dixon, N. (2019). *Géotechnique* **69**, No. 12, 1107–1122 [https://doi.org/10.1680/jgeot.18.P.209]

Acoustic emission behaviour of dense sands

ALISTER SMITH* and NEIL DIXON†

Interpretation of acoustic emission (AE) generated by particulate materials has to date been qualitative. The objective of this study was to move the discipline towards quantitative interpretation of AE to enable early warning of serviceability and ultimate limit state failures in the field, and to enhance the instrumentation of element and physical model tests in the laboratory. Results from a programme of drained triaxial tests on dense sands show that: AE generation is proportional to the imposed stress level, imposed strain rate, fabric coordination number and boundary work done; there are two types of AE response at the transition from contractive to dilative behaviour, which was governed by the mean particle size; and AE activity in particulate materials is negligible until the current stress conditions (compression and/or shear) exceed the maximum that has been experienced in the past. Relationships have been quantified between AE and boundary work (i.e. AE generated per Joule) for a unit volume of sand under isotropic compression and shear, and between AE and shear strain rate. An example interpretation framework demonstrates how AE measurements could be used to identify the transition from contractive to dilative behaviour, mobilisation of peak shear strength and quantify accelerating deformation behaviour that typically accompanies shear zone development.

KEYWORDS: consolidation; deformation; geophysics; laboratory tests; monitoring; sands

INTRODUCTION

Granular soils mobilise shearing resistance through inter-particle friction and interlocking (i.e. dilation, particle rearrangement and particle damage) (Sadrekarimi & Olson, 2011). Stresses applied to the boundary of a soil body are transmitted to the soil skeleton and cause normal and tangential forces to develop at particle contacts (Cundall & Strack, 1979; Senetakis *et al*., 2013). The orientation and distribution of particle contacts is typically referred to as the 'fabric', while the term 'state' is used to describe the soil's current physical condition and includes void ratio, stresses and fabric (Been & Jefferies, 1985; Been *et al*., 1991). The distribution and evolution of inter-particle forces at particle contacts strongly controls the mechanical behaviour of particulate systems (Wan & Guo, 2004).

Mobilisation of peak shear strength in dense sands typically causes shear strains to localise into concentrated shear zones with inclined column-like chains of particles and large void ratios (Hasan & Alshibli, 2010). Shear strength reduces in this post-bifurcation regime, as the sand approaches the critical state, and accelerating deformation behaviour typically ensues as the soil mass is weaker under the same imposed boundary stresses; this ultimate limit state can have devastating consequences for people and infrastructure.

Proportions of the energy dissipated during deformation of particulate materials are converted to heat and sound. The high-frequency (>10 kHz) component of this sound energy is called acoustic emission (AE). AE monitoring offers the potential to sense particle-scale interactions that lead to macro-scale responses of granular materials. AE is widely used in many industries for non-destructive testing and evaluation of materials and systems; however, it is seldom used in geotechnical engineering, despite evidence of the benefits, because AE generated by particulate materials is highly complex and difficult to measure and interpret.

AE is generated in particulate materials through a suite of mechanisms: particle–particle interactions such as sliding and rolling friction; particle contact network rearrangement (e.g. release of contact stress and stress redistribution as interlock is overcome and regained); degradation at particle asperities; and crushing (Michlmayr & Or, 2014; Smith *et al*., 2014).

Fundamental laboratory studies on the AE behaviour of soils carried out in the 1970s, 1980s and 1990s (e.g. Koerner *et al*., 1976, 1978, 1981, 1984; Tanimoto & Nakamura, 1981; Mitchell & Romeril, 1984; Tanimoto & Tanaka, 1986; Garga & Chichibu, 1990; Shiotani & Ohtsu, 1999) led to the following qualitative conclusions: well-graded soils generate more AE than uniformly graded soils; angular particles generate more AE than rounded particles; AE amplitude increases with particle size; higher imposed stresses generate greater AE activity; AE activity increases with imposed strain rate; soils exhibit greatly increased AE activity when stress levels exceed the pre-stress/pre-consolidation pressure due to the Kaiser effect (Lavrov, 2003); and AE activity increases with strain when densely packed arrangements of grains are sheared until the transition from contractive to dilative behaviour, whereupon the AE activity remains relatively constant. The research reported in this paper goes beyond the state-of-the-art and quantifies the influence of these variables upon AE generation for the first time.

The focus of AE research in geotechnical engineering over the past 60 years has been to quantify links between measured AE and soil strength and deformation behaviour to enable interpretation of the field performance of geotechnical infrastructure assets. Recent advances have been made in the interpretation of soil/structure interaction behaviour

Manuscript received 23 August 2018; revised manuscript accepted 4 January 2019. Published online ahead of print 5 February 2019. Discussion on this paper closes on 1 May 2020, for further details see p. ii.

* School of Architecture, Building and Civil Engineering, Loughborough University, Leicestershire, UK (Orcid:0000-0003-3363-300X).
† School of Architecture, Building and Civil Engineering, Loughborough University, Leicestershire, UK.

from AE measurements using physical modelling and field experiments. For slope monitoring applications, relationships between measured AE and slope deformation behaviour have been quantified, enabling early warning of accelerating slope movements and failure (Smith *et al.*, 2014, 2017; Smith & Dixon, 2015; Dixon *et al.*, 2015a, 2015b, 2018; Michlmayr *et al.*, 2017; Berg *et al.*, 2018). For pile monitoring applications, relationships between measured AE and load–displacement behaviour are being developed (Mao *et al.*, 2015, 2016, 2018a, 2018b).

Lin *et al.* (2018) recently observed that loose sands generated more AE than dense sands in triaxial tests, which is possibly due to the greater distribution of shear strains and hence particle dislocations within a bulging-type failure. These results are important and interesting, but are based on a limited number of tests and stress conditions (i.e. three tests at different relative densities and one effective confining stress). Mao & Towhata (2015) found that particle crushing has a much higher frequency content (>100 kHz) than inter-particle friction and particle rearrangement (<100 kHz). Ibraim *et al.* (2017) have investigated particle crushing-generated AE in uniaxial compression tests. In addition, numerical simulations with fibre-bundle models are being used to investigate the AE behaviour of grain-scale interactions (Michlmayr *et al.*, 2013; Michlmayr & Or, 2014). These studies demonstrate the benefits of AE monitoring, but do not provide methodologies to interpret and quantify soil behaviour from AE measurements.

Interpretation of the AE generated by particulate materials has to date been qualitative. The objective of this study was to move the discipline towards quantitative interpretation of AE to enable early warning of serviceability and ultimate limit state failures in the field, and to enhance the instrumentation of element and physical model tests in the laboratory. A programme of drained triaxial isotropic compression and shearing tests was performed on dense sands to investigate the influence of volume change behaviour, stress level, stress history, strain rate and work done by boundary stresses.

METHODOLOGY

Apparatus

Triaxial tests enabled the systematic investigation of the evolution of AE with the stress–strain response of dense sands at a range of effective confining stresses and strain rates under drained conditions. The triaxial test remains the most widely used element test, in research and practice, for simulating conditions on soil specimens. The authors acknowledge that dense sands can remain dilatant at the end of a test and not reach the critical state (i.e. constant volume) due to the limited magnitude of strain that can be imposed (Been *et al.*, 1991; Sadrekarimi & Olson, 2011; López-Querol & Coop, 2012). However, the final dilation rate ($\delta\varepsilon_{vol}/\delta\varepsilon_{\gamma}$) measured at the end of the tests reported here ranged from 0 to 0·04 for the smallest and largest mean particle sizes, respectively.

A hydraulic GDS Instruments (Hook, UK) Bishop & Wesley (1975) stress path triaxial apparatus was used to eliminate the noise that could be generated by motor-operated systems. A schematic diagram of the apparatus is shown in Fig. 1; the apparatus has a bespoke 50 mm dia. base pedestal incorporating both AE and pore-water pressure measurement.

Soils

Quartz Leighton Buzzard sand (LBS) was selected for this investigation as its mechanical behaviour has been studied extensively in the literature (e.g. Cavarretta *et al.*, 2011; Senetakis *et al.*, 2013) and batches of different size fractions could be procured with consistent properties. Four uniformly graded size fractions were selected to minimise the influence of different fabrics and control, as far as is practically possible with a natural sand, mineralogy, shape, surface roughness and inter-particle friction. In addition, a fifth sand, 'LBS combined', was created by combining the four uniformly graded fractions to investigate the influence of a significant change to fabric and void ratio.

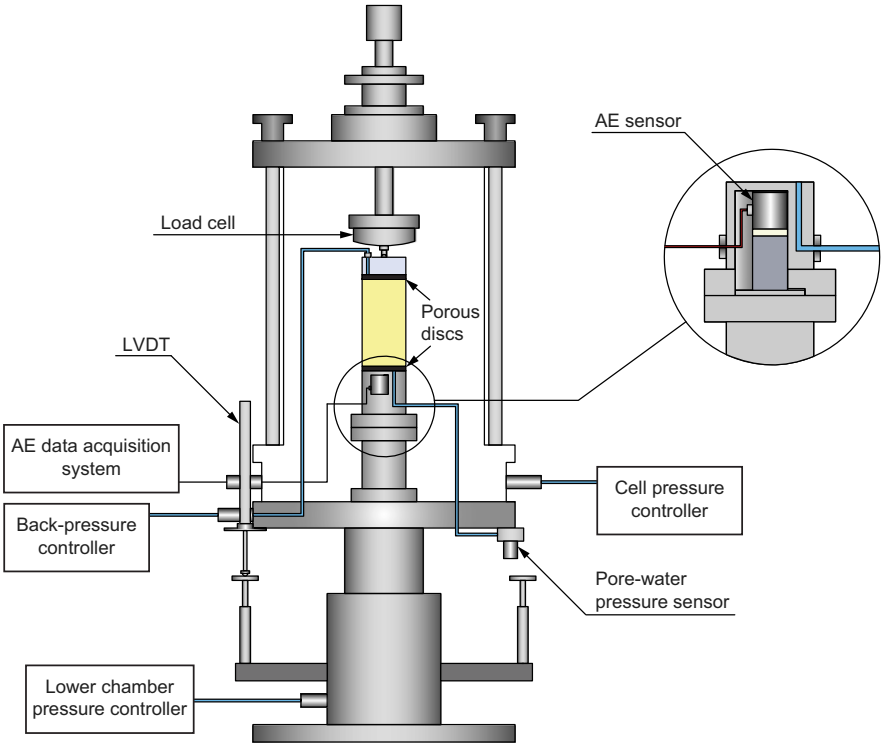

Fig. 1. Schematic diagram of the GDS Instruments Bishop and Wesley stress path triaxial apparatus and modified base pedestal to incorporate both AE and pore-water pressure measurement. LVDT, linear variable differential transformer

Table 1. Physical properties of the quartz LBS

Description	Particle size			Packing				Particle shape				Mohs hardness	Inter-particle friction
									Sphericity	Roughness			
	Size range: mm	C_u	C_c	ρ_s	$\rho_{dry_{min}}$	$\rho_{dry_{max}}$	e_{min}	e_{max}	Roundness				ϕ_μ
										R_a: μm	R_q: μm	R_z: μm	
Leighton Buzzard sand													
LBS 5/8	2·00–3·35	1·344	0·964	2·682	1·580	1·760	0·524	0·698	0·18–0·73 (mean = 0·48)	0·36–0·86 (mean = 0·63)	0·25–10·56 (mean = 1·70)	0·32–12·89 (mean = 2·37)	1·24–44·68 (mean = 8·29)	6·0–7·0	20°–23° (Cavarretta *et al.*, 2011)
LBS 8/16	1·00–2·00	1·787	1·158	2·670	1·530	1·724	0·548	0·744							
LBS 14/25	0·6–1·18	1·462	0·935	2·653	1·504	1·720	0·542	0·764							
LBS 2EW	0·25–0·71	1·656	1·090	2·761	1·551	1·773	0·558	0·781							
LBS Combined	0·25–3·35	3·11	0·89	2·691	1·664	1·803	0·492	0·617							

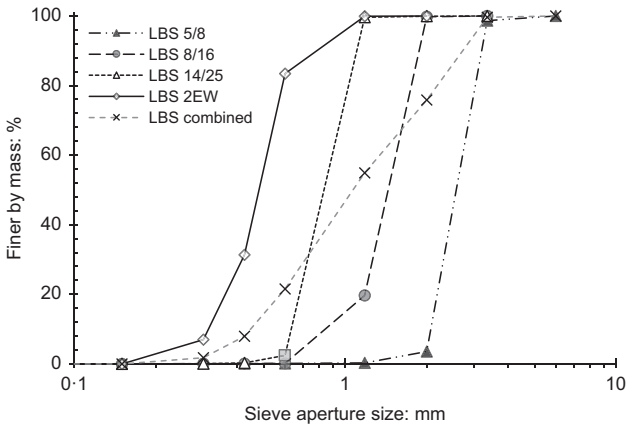

Fig. 2. Particle size distributions of the LBS

The physical properties of the LBS are shown in Table 1 and their particle size distributions are shown in Fig. 2. Particle size and packing properties were quantified using soil testing methods to BS EN ISO 17892 (BSI, 2016). The reported particle shape parameters (range and mean) are the result of measurements from 40 particles taken across the four particle size ranges. Roundness and sphericity were computed using the method described in Zheng & Hryciw (2015) from two-dimensional (2D) microscope images of the particles. Roundness is quantified as the average radius of curvature of particle surface features relative to the radius of the largest circle that can be inscribed in the particle. Sphericity (circle ratio) is quantified as the diameter ratio between the largest inscribing and smallest circumscribing circles (Krumbein & Sloss, 1963; Cho *et al.*, 2006; Cavarretta *et al.*, 2010; Zheng & Hryciw, 2015). Roughness was computed using high-resolution optical three-dimensional (3D) measurements of the particles acquired with an Alicona infinite focus system. Roughness parameters R_a, R_q and R_z are the roughness average, root mean square roughness and average maximum profile height, respectively. Scanning electron microscope (SEM) images of an LBS particle are shown in Fig. 3.

Testing procedure

Specimen preparation followed a similar procedure to that described in Been *et al.* (1991). The cylindrical specimens were 50 mm in diameter and 100 mm tall. Samples were prepared in a membrane-lined split-mould mounted on the base pedestal. Moist compacted samples were tamped into the mould to a target relative density, D_r, of approximately 85% in ten equal layers. Back-pressure saturation (Head, 1986; Been *et al.*, 1991; Sadrekarimi & Olson, 2011) of 400 kPa was imposed under a constant effective stress of approximately 20 kPa until a minimum pore-pressure parameter, B, of 0·97 was measured (Skempton, 1954). Back-pressure of 400 kPa was maintained throughout the subsequent test stages.

Isotropic compression was performed by increasing the cell pressure to achieve a target effective stress (e.g. 100, 200 or 300 kPa), which led to excess pore-water pressure generation and consolidation. The shearing stage was initiated after no further volume change took place and 100% of the excess pore-water pressure had dissipated.

Shearing was performed in a strain-controlled manner through application of a constant rate of axial displacement. Axial displacement rates of 1, 3 and 6 mm/h were applied to ensure drained conditions (i.e. any excess pore-water pressures (<2 kPa) were observed to dissipate rapidly, and hence the effective confining stress was constant). The appropriate

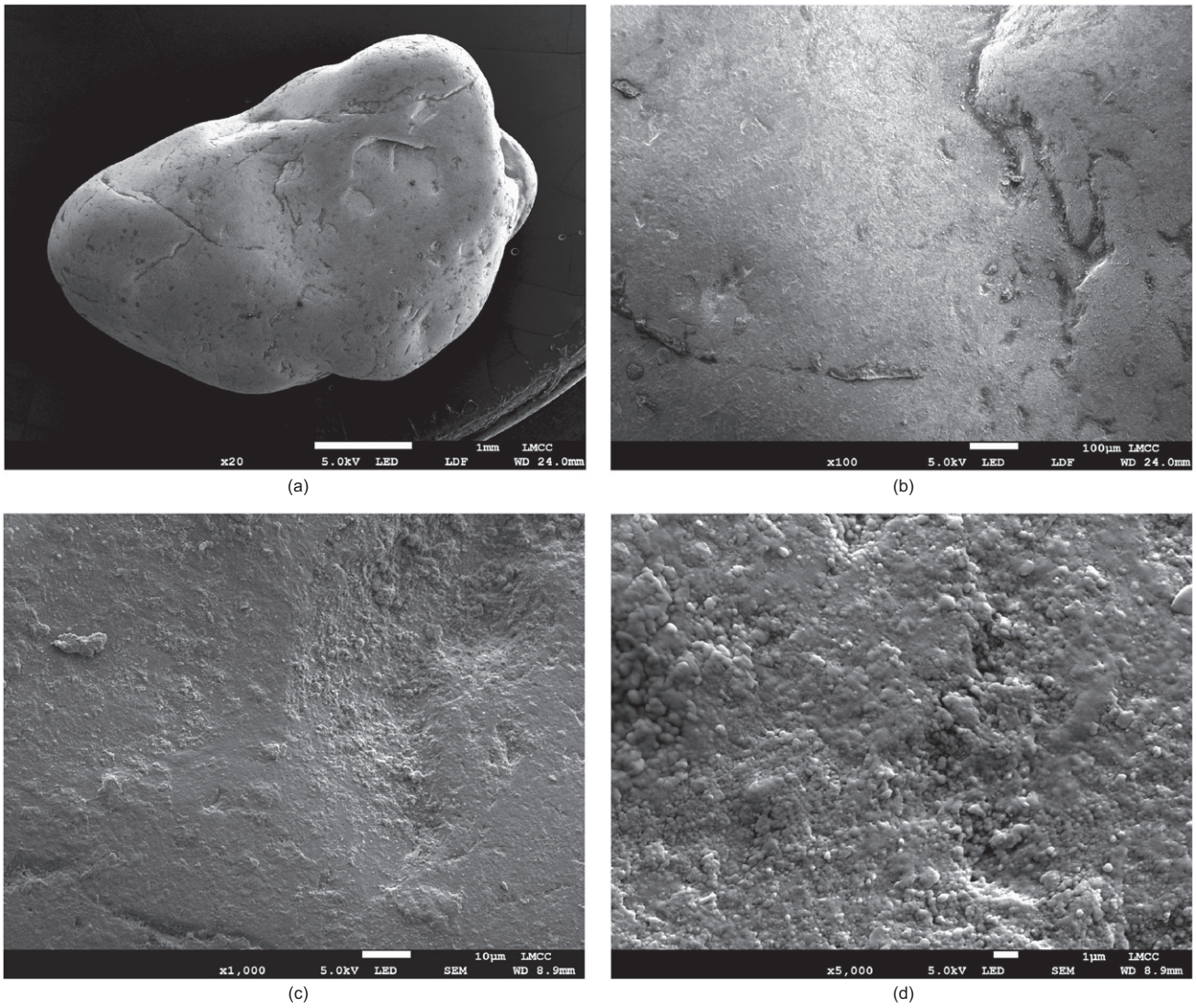

Fig. 3. Scanning electron microscope (SEM) images of a LBS particle. The length of the white bar in the bottom panel of each image shows the scale: 1 mm in (a), 100 μm in (b), 10 μm in (c) and 1 μm in (d)

corrections for the membrane and changes in specimen area were applied to the measurements (Head, 1986).

A summary of the triaxial tests performed in this investigation is shown in Table 2. The state parameter, ψ, is the difference in void ratio between the current state and that on the critical state line at the current mean effective stress (reported for the onset of shearing in Table 2). Additional parameters describing the fabric and stress anisotropy are also necessary to define the unique state of a sand, but these are difficult to measure and rarely available (Been & Jefferies, 1985). The peak and critical state friction angles obtained were comparable for each of the four uniformly graded sands (±1°). The critical state friction angles obtained are typical and consistent with those reported by Bolton (1986) for quartz sands (i.e. 33° ± 1°).

Energy calculations

Equations (1)–(3) were used to quantify the work done during the triaxial experiments for comparison with AE measurements. The increment of work done per unit volume transmitted to the soil skeleton across its boundaries (i.e. boundary work) was computed using equation (1). Boundary work per unit volume has two components: distortional work per unit volume, which causes a change of sample shape (equation (2)); and volumetric work per unit volume, which causes a change of sample volume (equation (3)) (Muir Wood, 1990; Bolton, 2003; Powrie, 2013; Hanley *et al.*, 2017).

$$\Delta W = \Delta W_{\mathrm{d}} + \Delta W_{\mathrm{v}} \tag{1}$$

$$\Delta W_{\mathrm{d}} = q\delta\varepsilon_{\mathrm{q}} = \frac{2}{3}q\delta\varepsilon_{\gamma} \tag{2}$$

$$\Delta W_{\mathrm{v}} = p'\delta\varepsilon_{\mathrm{vol}} \tag{3}$$

where $\delta\varepsilon_{\gamma}$, $\delta\varepsilon_{\mathrm{q}}$ and $\delta\varepsilon_{\mathrm{vol}}$ are increments of shear strain, deviatoric strain and volumetric strain, respectively. The increments of work done per unit volume were multiplied by the current sample volume in each increment (Hanley *et al.*, 2017). This allowed direct comparison with the AE generated by each sample, and hence the AE generated for an increment of work done per unit volume.

Coordination number

A general estimation of how the microstructure in particulate materials evolves during shear can be conveyed from the average coordination number (CN) of the system

Table 2. Summary of the drained triaxial isotropic compression and shearing tests performed in this study

Test no.	Material*	σ'_r: kPa†	Axial displacement rate: mm/h	Initial D_r: %‡	ψ§	CN‖	AE behaviour type in shear	ϕ'_p**	ϕ'_{cv}**	M**
1	LBS 0·25–0·71	100	1	83·6	−0·156	8·57	1	42°	34°	1·37
2	LBS 0·25–0·71	200	1	83·6	−0·132	8·62	2			
3	LBS 0·25–0·71	300	1	83·6	−0·112	8·63	2			
4	LBS 0·6–1·18	100	1	83·5	−0·132	8·60	2	41°	33°	1·33
5	LBS 0·6–1·18	200	1	83·5	−0·110	8·64	2			
6	LBS 0·6–1·18	300	1	83·5	−0·102	8·68	2			
7	LBS 1·0–2·0	100	1	84·1	−0·153	8·75	1	41°	34°	1·37
8	LBS 1·0–2·0	200	1	84·1	−0·129	8·80	1			
9	LBS 1·0–2·0	300	1	84·1	−0·114	8·84	1			
10	LBS 1·0–2·0	300	3	84·1	−0·114	8·84	1			
11	LBS 1·0–2·0	300	6	84·1	−0·114	8·84	1			
12	LBS 2·0–3·35	100	1	83·1	−0·143	8·81	1	41°	34°	1·37
13	LBS 2·0–3·35	200	1	83·1	−0·116	8·82	1			
14	LBS 2·0–3·35	300	1	83·1	−0·103	8·86	1			
15	LBS 0·25–3·35	300	1, 3, 6	82·4	—	9·29	2	—		
16††	LBS 1·0–2·0	300	6	84·1	−0·114	8·84	1	—		

*Material identified using the size range shown in Table 1.
†Final effective confining pressure after isotropic compression and constant during shearing.
‡Initial relative density prior to isotropic compression.
§State parameter at onset of shearing (i.e. after isotropic compression). Note that the critical state lines in e–p' space, and hence the state parameters, were interpreted from the final void ratio at the end of each test, but dilation can continue in dense sands beyond 20% axial strain (Been *et al.*, 1991).
‖Average coordination number at onset of shearing (i.e. after isotropic compression).
**Friction parameters obtained from drained triaxial shearing tests performed in this study at three different cell pressures.
††Isotropic load–unload–reload (LUR) cycles of cell pressure followed by LUR cycles of deviator stress.
Note: All specimens failed with a concentrated shear zone in shearing.

(Mirghasemi *et al.*, 2002). The CN refers to the average number of contacts per particle and is a measure of the fabric of granular materials (Oda, 1977; Cui & O'Sullivan, 2006; Hasan & Alshibli, 2010). The following linear relationship between e and CN has been reported in the literature based on experimental data for granular materials (Chang *et al.*, 1990; Hasan & Alshibli, 2010)

$$e = 1{\cdot}66 - 0{\cdot}125\text{CN} \quad \text{for} \quad 0{\cdot}38 \leq e \leq 0{\cdot}87 \tag{4}$$

The CN for each material was calculated using equation (4) in the research reported here to investigate the influence of the number of contacts per particle on AE generation. AE generation following mobilisation of peak shear strength in dense sands is controlled by shear deformation within a concentrated, dilating shear zone. The local void ratio within this shear band is much greater than the global void ratio (i.e. average for the specimen) (Desrues *et al.*, 1996). Although more significant fabric changes will have occurred in the shear zone than those calculated using the global void ratio, general trends and relationships between CN and AE generation can be obtained.

The CN has been shown to vary proportionally with volumetric strain during shearing of dense granular materials, that is CN initially increases as the soil contracts and reaches a maximum at the transition from contractive to dilative behaviour, then reduces as the sand dilates at a rate proportional to the dilatancy, and stabilises at constant volume (e.g. Mirghasemi *et al.*, 2002; Cui *et al.*, 2007).

Acoustic emission measurements

A body of research has demonstrated that deforming soils generate significant AE within the frequency range of 10–100 kHz (e.g. Koerner *et al.*, 1981; Michlmayr *et al.*, 2013; Naderi-Boldaji *et al.*, 2017; Smith *et al.*, 2017). Filtering signals below 10 kHz is essential to remove extraneous low-frequency environmental noise that could be generated in a laboratory by machinery or in a field environment by construction activity or traffic. Soil-generated AE can have energy at frequencies below 10 kHz; however, noise can significantly contaminate the measurements at these frequencies, which requires arduous processing to remove. Filtering signals above 100 kHz is appropriate as the study focused on relatively low effective confining stresses (from 100 to 300 kPa) and particle damage was minimal (confirmed from post-test particle size distributions) (Mao & Towhata, 2015).

The AE sensor was installed inside the base pedestal, as shown in Fig. 1; a 5 mm wall of stainless steel separated the surface of the sensor and the top surface of the pedestal. Measuring AE at this consistent position eliminated sensor location and coupling quality as variables from the investigation. Moreover, installation of AE sensors at this position

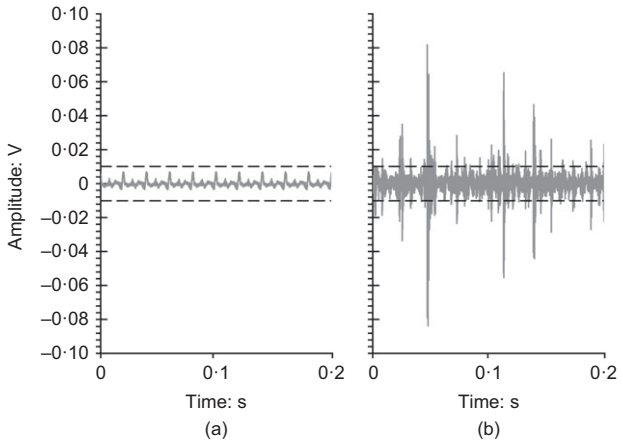

Fig. 4. Example waveforms recorded using the AE measurement system showing the 0·01 V threshold level: (a) background environmental and electronic noise; (b) during soil deformation

is more practicable for routine element testing than direct on-sample coupling. The sensor was a Mistras Group (Cambridge, UK) R3α piezoelectric transducer, which is sensitive over the frequency range of 0–100 kHz and has a resonant frequency of 30 kHz. The sensor converts the mechanical AE to a voltage waveform that can be processed.

The AE measurement system was a bespoke set-up comprising a pre-amplifier (with a 10–1200 kHz filter and 20 dB gain), a main amplifier (with a 10–100 kHz filter and 3 dB gain), an analogue-to-digital converter with 2 MHz sampling frequency and a laptop with a LabView program to condition, process and record the AE waveform. The two amplifiers were used to improve the signal-to-noise ratio. The LabView program was set to further attenuate signals outside the 10–100 kHz range and record the full AE waveform within this frequency range.

Two key AE parameters of interest are ring-down counts (RDC) and *b*-value. RDC per unit time are the number of times the AE waveform crosses a programmable threshold level (set to 0·01 V in this study, above background environmental and electronic noise, as shown in Fig. 4) within a predefined time interval and are a measure of the signal energy. The *b*-value can be obtained from the full AE waveform data (Pollock, 1973) and is a convenient way to describe the amplitude distribution in a single value. When the AE waveform is dominated by low-amplitude events the *b*-value is large. As the proportion of higher amplitude events increases, indicating an increase in energy, the *b*-value reduces. The *b*-value was computed at 1 min intervals using equations (5) and (6).

$$\log N = c - bm \tag{5}$$

$$m = \log A \tag{6}$$

where A is the amplitude; m is a log-scale measure termed magnitude; N is the number of AE events with magnitude greater than m; c is the point where the log(N) plotted against

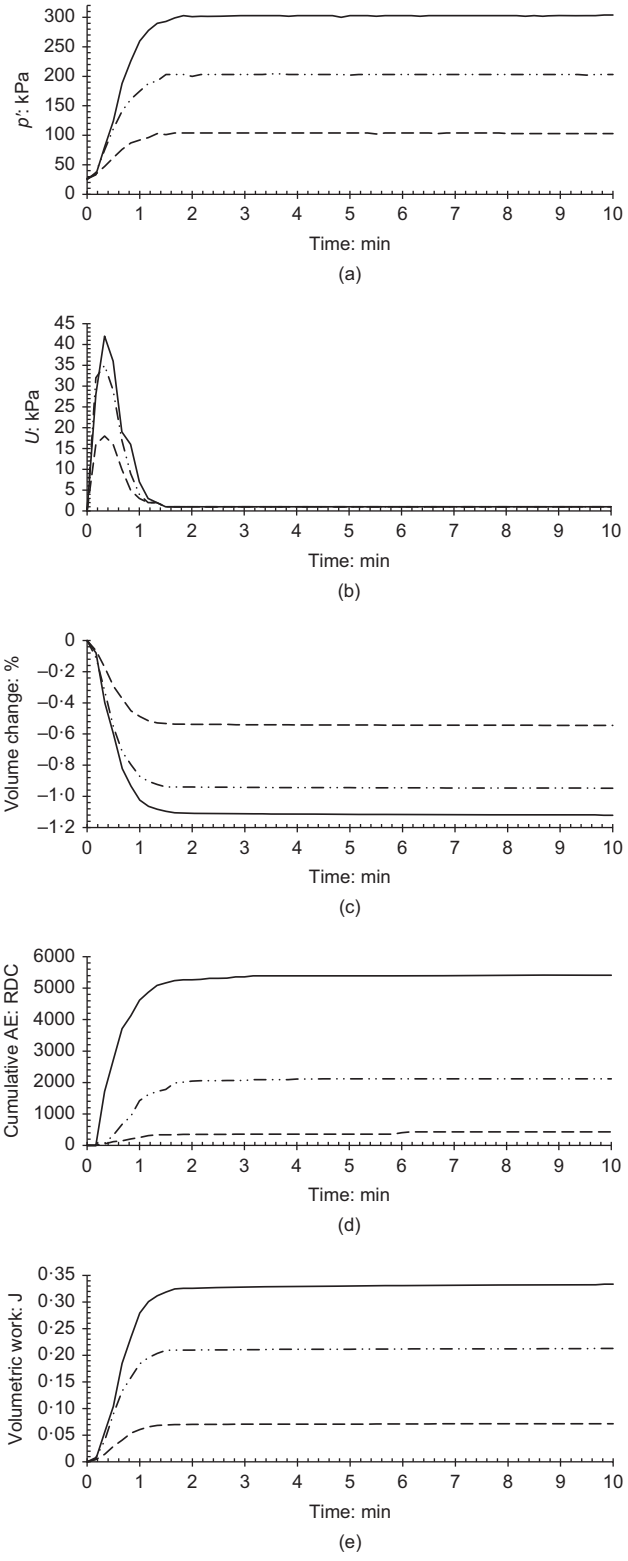

Fig. 5. Time series measurements from isotropic compression tests to effective confining pressures of 100, 200 and 300 kPa performed on LBS 0·6–1·18 (tests 4, 5 and 6): (a) mean effective stress; (b) excess pore-water pressure; (c) volume change (%); (d) cumulative AE (RDC); (e) cumulative volumetric work (J)

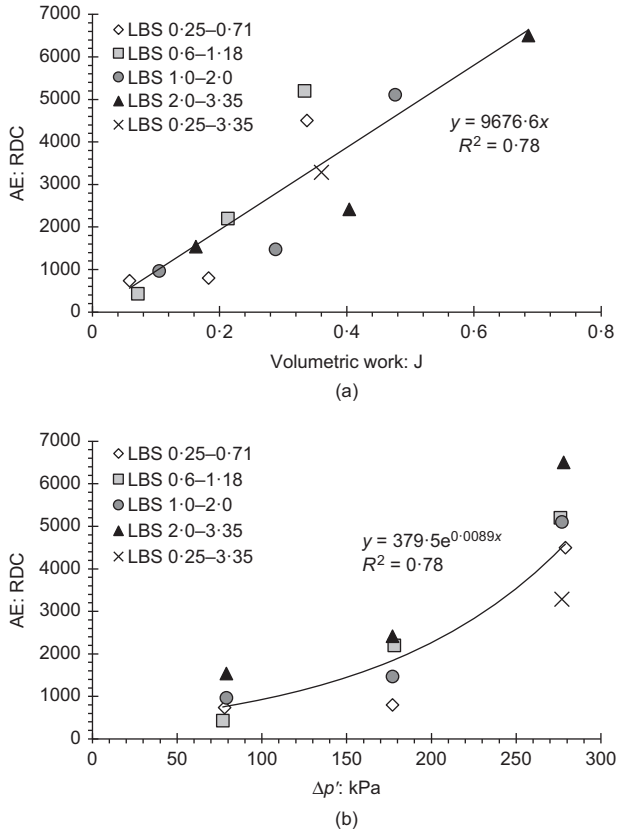

Fig. 6. Results from isotropic compression tests to effective confining pressures of 100, 200 and 300 kPa performed on LBS (tests 1–9 and 12–15): (a) total generated AE (RDC) plotted against the total volumetric work done (J); (b) total generated AE plotted against the change in mean effective stress (kPa)

m relationship intersects the *y*-axis; and the coefficient *b* (*b*-value) is the negative slope of the log(*N*) plotted against *m* relationship.

RESULTS

Isotropic compression

Figure 5 shows example time series measurements from isotropic compression performed on LBS 0·6–1·18 (tests 4, 5 and 6). Space precludes inclusion of time series measurements for all tests; however, the general trends in behaviour were the same, and the results from all isotropic compression tests (tests 1–9 and 12–15) are compared in relation to the volumetric work done and change in mean effective stress in Fig. 6.

An increase in cell pressure caused excess pore-water pressures to develop, which dissipated as the sample consolidated and the mean effective stress increased. The cumulative RDC generated was proportional to the change in mean effective stress and magnitude of volumetric work done, and they followed comparable trends with time (Figs 5(a), 5(d) and 5(c)).

The linear regression plotted through results from all LBS (tests 1–9 and 12–15) in Fig. 6(a) shows that, in general, approximately 10 000 RDC were generated per 1 J of volumetric work done. Fig. 6(b) shows the relationship between generated RDC and the change in mean effective stress, which is best described using the exponential function (highest R^2 obtained from systematic curve fitting of 0·78) for the range of data reported.

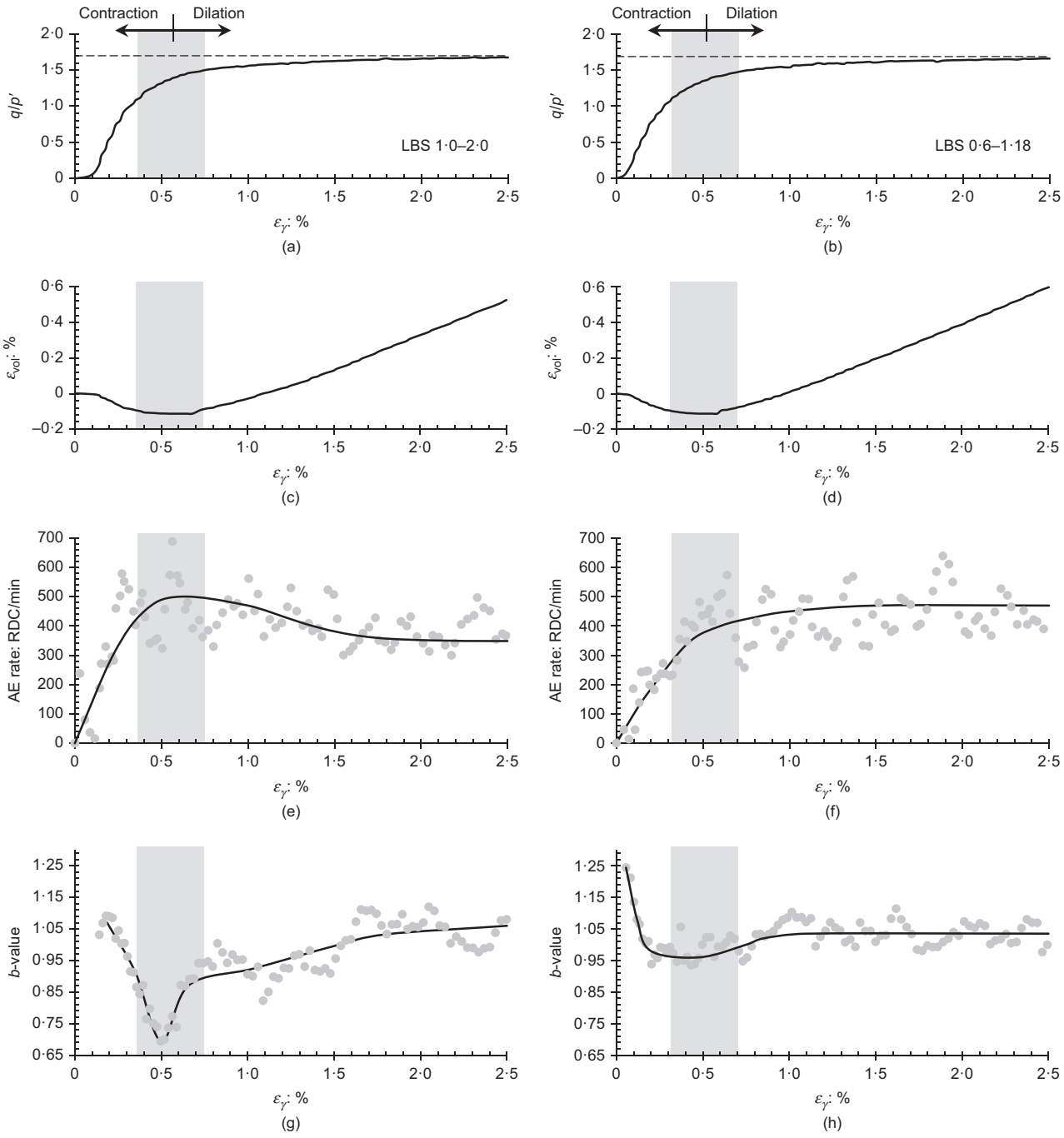

Fig. 7. Example measurements plotted against shear strain (%) from drained triaxial shearing tests performed on LBS 1·0–2·0 (test 8, left) and LBS 0·6–1·18 (test 5, right) at an effective confining pressure of 200 kPa and axial displacement rate of 1 mm/h: (a), (b) stress ratio (*q*/*p*′); (c), (d) volumetric strain (%) (dilation shown as positive); (e), (f) AE rate (RDC/min); (g), (h) *b*-value

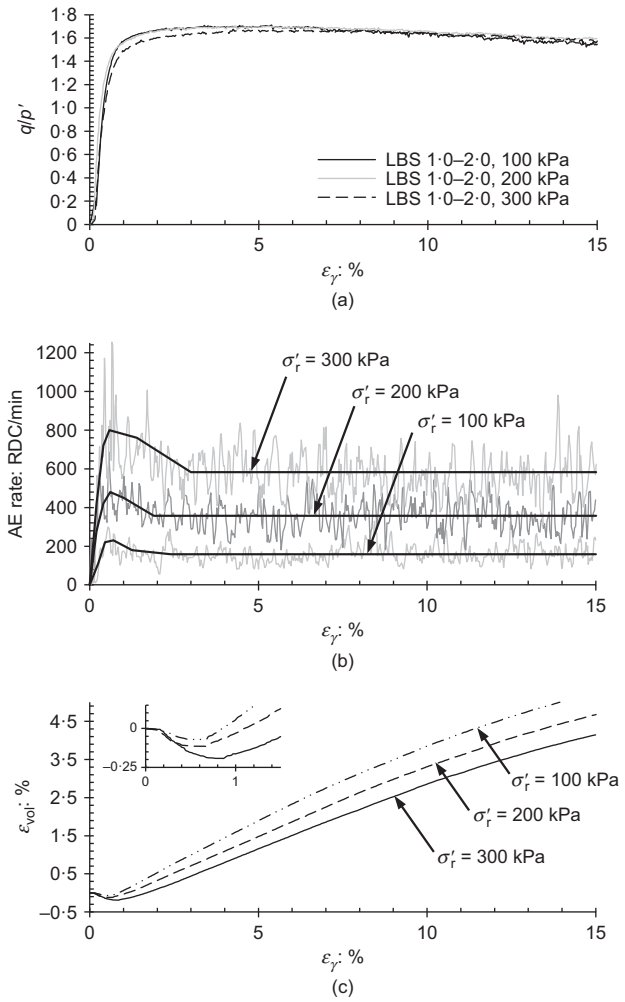

Fig. 8. Measurements plotted against shear strain (%) from drained triaxial shearing tests performed on LBS 1·0–2·0 at effective confining pressures of 100, 200 and 300 kPa and axial displacement rate of 1 mm/h (tests 7, 8 and 9): (a) stress ratio (q/p'); (b) AE rate (RDC/min); (c) volumetric strain (%) (dilation shown as positive)

As the magnitude of mean effective stress increases, and hence the volume of the sample decreases, the CN increases. The combined effect of both stress change and CN change is therefore the cause of the exponential, as opposed to linear, relationship. Moreover, the change in CN is likely to be the main cause for the scatter in Fig. 6(a) (R^2 of 0·78) (e.g. AE generated by each material increased exponentially, as opposed to linearly, with volumetric work in Fig. 6(a)). Other potential reasons for variability include: natural variations in the particles (e.g. shape and roughness); differences in initial fabric (e.g. the same sands with equal void ratio and confining stress have been observed to exhibit different stress–strain behaviour due to differences in initial fabrics derived from sample preparation (Arthur & Menzies, 1972; Oda, 1972; Been & Jefferies, 1986)); the rate of consolidation (i.e. rate of volume change and hence particle–particle interactions); and differences in propagation paths and attenuation through the soil skeleton as the AE waves travelled from the generation sources to the sensor.

Shearing

Figure 7 shows measurements plotted against shear strain from test 8 (LBS 1·0–2·0) and test 5 (0·6–1·18) to exemplify the two types of AE behaviour observed in this study. All tests exhibited one of these two trends in behaviour, and the AE behaviour type experienced by each is detailed in Table 2. AE activity increases (i.e. AE rates increase, and b-values reduce) approximately linearly with shear strain in both identified types of behaviour until the point of volume minimum (i.e. transition from contractive to dilative behaviour). In addition, AE activity remains relatively constant following mobilisation of peak shear strength in both behaviour types. The difference in behaviour occurs between the point of volume minimum and mobilisation of peak shear strength: type-1 (illustrated by LBS 1·0–2·0) exhibits a significant peak in AE activity at the point of volume minimum, which then reduces and stabilises at peak shear strength; type-2 (illustrated by LBS 0·6–1·18) does not exhibit a significant peak and drop in AE rates but does exhibit a trough in b-value measurements at the point of volume minimum, although significantly less in magnitude than type-1.

AE is generated by particle-scale interactions and evolving mechanisms such as inter-particle friction, slip–stick and particle rearrangement, and hence the AE measurements have a variable nature. Smoothed curves of moving average values have been used to describe the general trends.

Figure 8 shows measurements plotted against shear strain from tests 7, 8 and 9 (LBS 1·0–2·0) to demonstrate the influence of stress level. An increase in effective confining pressure caused a proportional increase in AE rates, and a greater range of shear strain before constant AE rates were reached (i.e. consistent with the volumetric strain behaviour at volume minimum, whereby contraction was extended over a greater range of shear strain). AE rates increase with confining pressure because greater inter-particle contact stresses develop, and hence more work is required to displace particles relative to each other. Although post-test particle size distributions did not reveal any significant particle crushing, it is also possible that particle damage caused elevated AE activity at higher confining stresses. The b-value measurements were not significantly modified by stress level; however, they were influenced by shear strain rate (described later).

Figure 9(a) compares the average AE rates measured at volume minimum and post-peak ($\varepsilon_\gamma = 20\%$) for tests 1–9 and 12–15 (axial displacement rate of 1 mm/h) to illustrate the influence of stress level and mean particle size, and to identify type-1 and type-2 AE behaviours. A general trend of increasing AE rates with stress level and mean particle size can be observed. The difference in AE rates between volume minimum and post-peak are shown in Fig. 9(b), which indicates that the AE behaviour type was generally governed by mean particle size.

AE activity at peak dilatancy (i.e. q/p'_{max}) is compared in Fig. 10 for tests 1–9 and 12–15 (axial displacement rate of 1 mm/h). Fig. 10(a) shows a general trend of AE rates increasing with imposed effective confining pressure. Linear and power function regressions result in R^2 values of 0·70 and 0·77, respectively, for the range of data reported. Normalising AE rates by stress level (i.e. using the linear AE rate plotted against confining stress relationship) allows the influence of other variables to be investigated; Fig. 10(b) shows the measured AE rates normalised by the effective confining pressure plotted against the peak dilation rate, which exhibits an inverse linear relationship. Dilatancy becomes more restricted at higher confining stresses, which reduces the change in void ratio and CN, and hence AE generation generally increased as the dilation rate reduced.

Figure 11 shows measurements plotted against shear strain from tests 9, 10 and 11 (LBS 1·0–2·0) to demonstrate the influence of axial displacement rate. AE rates increased proportionally with the imposed displacement rate as more

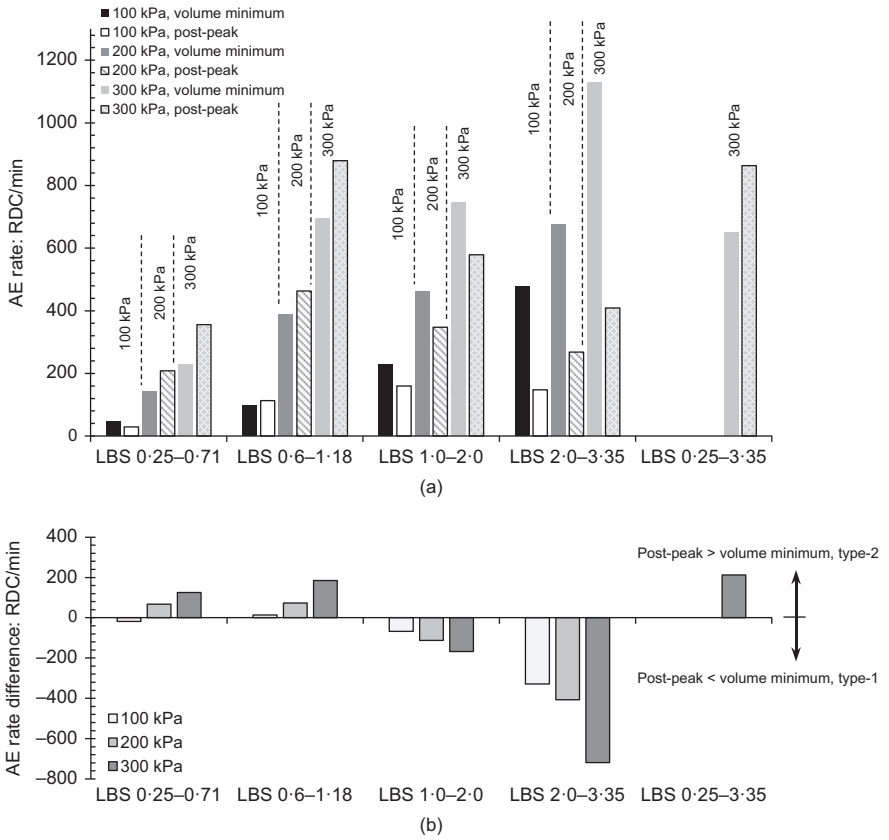

Fig. 9. Results from drained triaxial shearing tests at effective confining pressures of 100, 200 and 300 kPa performed on LBS at an axial displacement rate of 1 mm/h (tests 1–9 and 12–15): (a) average AE rate (RDC/min) measured at volume minimum (i.e. transition from contractive to dilative behaviour) and average AE rate (RDC/min) measured after mobilisation of post-peak shear strength at 20% shear strain; (b) differences between the average AE rates measured at volume minimum and post-peak

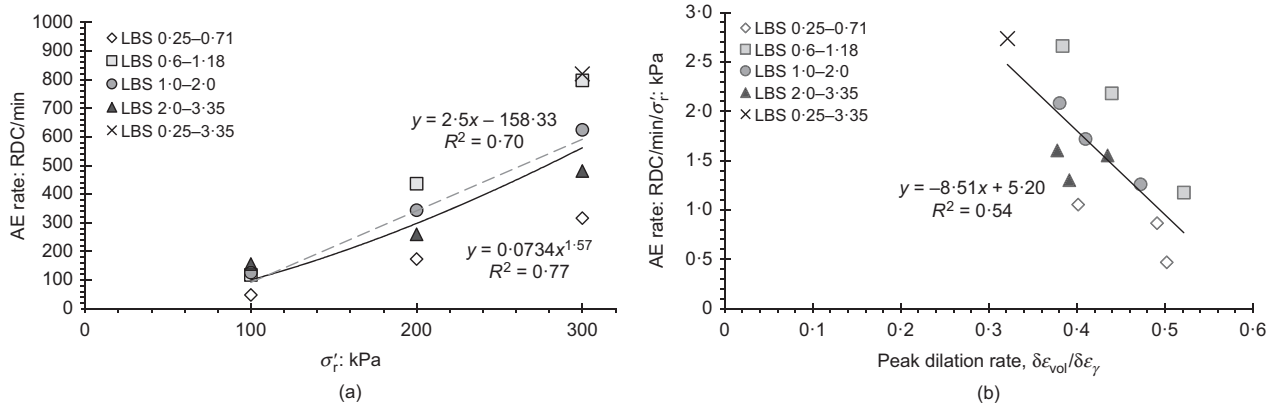

Fig. 10. Results from drained triaxial shearing tests at effective confining pressures of 100, 200 and 300 kPa performed on LBS at an axial displacement rate of 1 mm/h (tests 1–9 and 12–15): (a) average AE rate (RDC/min) measured at peak dilatancy (i.e. q/p'_{max}) plotted against effective confining pressure; (b) average AE rate (RDC/min) measured at peak dilatancy normalised by the mean effective confining pressure plotted against dilation rate

particle-scale interactions took place per unit time; average post-peak AE rates for 6 mm/h and 3 mm/h were 5·7 and 3·3 times greater than those generated at 1 mm/h, respectively (i.e. very close to theoretical ratios of 6 and 3, respectively, based on the work done per unit time in each test). The average post-peak *b*-values were 0·90, 0·79 and 0·68 for displacement rates of 1, 3 and 6 mm/h, respectively.

Results from test 15 (LBS 0·25–3·35) are shown in Fig. 12. Stepped increases in axial displacement rate were imposed during the test when post-peak conditions were established to investigate the AE response to accelerating deformation behaviour. The average post-peak AE rates for 6 mm/h and 3 mm/h were 6·2 and 2·8 times greater than those generated at 1 mm/h, respectively (again very close to ratios of 6 and 3, respectively, Fig. 12(c)), and with relatively constant AE generation per increment of boundary work (Fig. 12(e)). The average post-peak *b*-values were 0·622, 0·537 and 0·415 for displacement rates of 1, 3 and 6 mm/h, respectively. These *b*-values are significantly lower, indicating a higher proportion of higher magnitude events, than those measured for the four uniformly graded sands, which had lower CN than LBS 0·25–3·35 (e.g. Table 2).

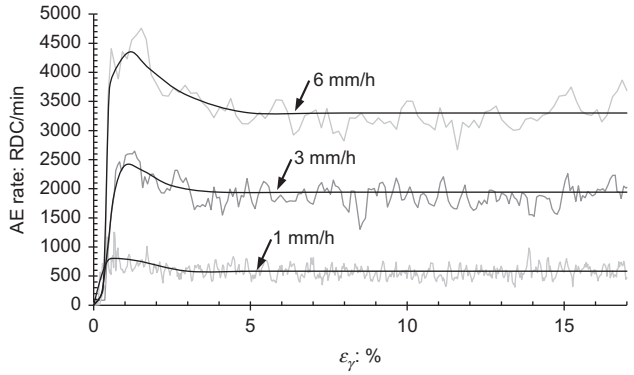

Fig. 11. AE rate (RDC/min) plotted against shear strain (%) measurements from drained triaxial shearing tests performed on LBS 1·0–2·0 at 300 kPa effective confining pressure and axial displacement rates of 1, 3 and 6 mm/h (tests 9, 10 and 11)

AE rate and *b*-value plotted against shear strain rate relationships obtained for LBS 1·0–2·0 and LBS 0·25–3·35 (tests 9, 10, 11 and 15) are presented in Fig. 13, which have strong correlation with R^2 values ranging from 0·96 to 0·99. Relationships for LBS 1·0–2·0 are presented for volume minimum, peak dilatancy and post-peak ($\varepsilon_\gamma = 20\%$) using results from tests 9–11, whereas relationships for LBS 0·25–3·35 are presented for post-peak only using results from test 15 (Fig. 12). The LBS 1·0–2·0 relationships for volume minimum show greater AE activity (higher AE rates and lower *b*-values) than those for peak dilatancy and post-peak, which are comparable. The post-peak LBS 0·25–3·35 AE rate–shear strain rate relationship is comparable to the volume minimum LBS 1·0–2·0 relationship. Significantly lower *b*-values were generated by LBS 0·25–3·35 than LBS 1·0–2·0.

Figure 14 compares AE (RDC) measurements with work done (boundary, distortional and volumetric) during all tests performed on LBS 1·0–2·0 (tests 7–11) (i.e. under different imposed effective confining stresses and axial displacement rates). The AE generated per increment of boundary work (RDC/J) plotted again shear strain (Fig. 14(e)) is comparable for all five tests: all exhibit elevated RDC/J at volume minimum, which then gradually reduces as peak shear strength is mobilised and then remains relatively constant (i.e. type-1 AE behaviour) at around 20 000 RDC/J.

The average AE rate plotted against boundary work rate relationships for tests 1–15 are compared in Fig. 15 for volume minimum (Fig. 15(a)), peak dilatancy (Fig. 15(b)) and post-peak (Fig. 15(c)). Regressions with R^2 values ranging from 0·89 to 0·98 were obtained for the relationships that include data for the higher displacement rates (3 and 6 mm/h), while R^2 values ranging from 0·58 to 0·73 were obtained when the higher displacement rate data were excluded (insets in Fig. 15). The gradient of the relationship for volume minimum is significantly greater than those for peak dilatancy and post-peak. These relationships also demonstrate that the sands generated significantly greater AE per unit of imposed boundary work in shear than they did in isotropic compression (e.g. Fig. 6(a), discussed later).

Figures 16 and 17 show the relationships between AE generation and CN at volume minimum, peak dilatancy and post-peak. AE rates are normalised by the current mean effective stress in Fig. 16, which highlights the significant increase in AE rates when the imposed displacement rate increased (the linear regressions presented in Fig. 16 exclude data from the higher displacement rates). Fig. 17 shows the AE generated per increment of boundary work (RDC/J). All linear regressions show positive correlation, with R^2 values

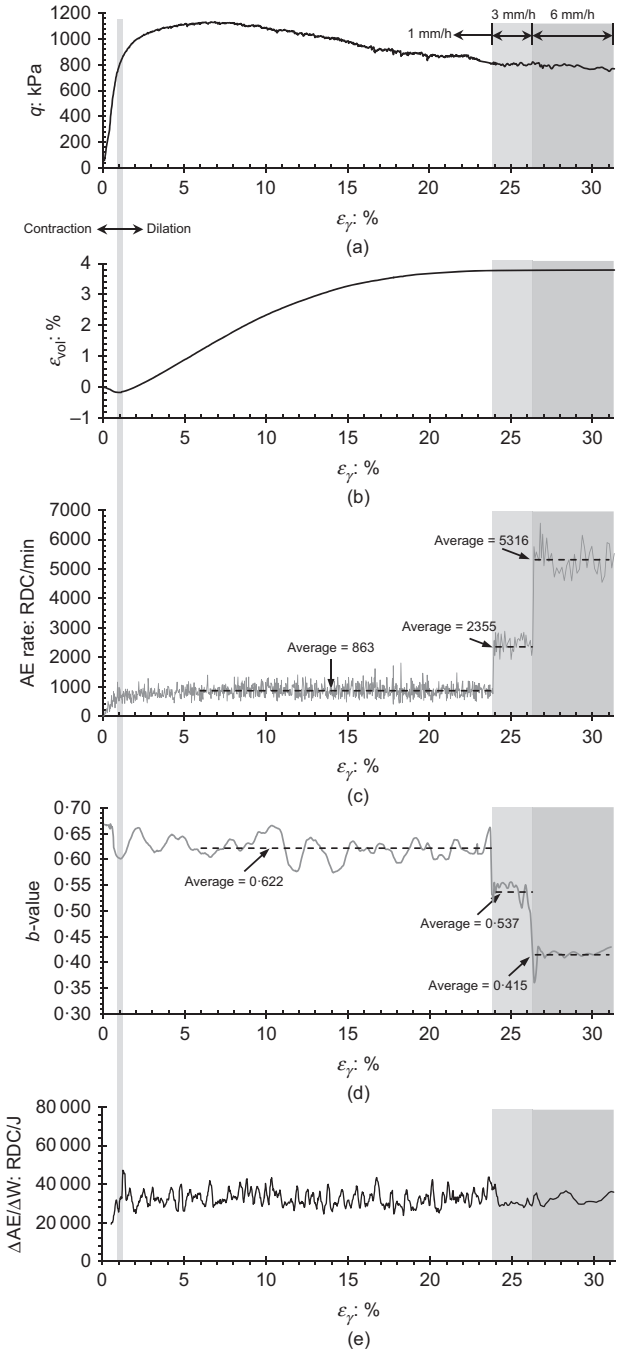

Fig. 12. Measurements plotted against shear strain (%) from a drained triaxial shearing test performed on LBS 0·25–3·35 at an effective confining pressure of 300 kPa and axial displacement rates of 1, 3 and 6 mm/h (test 15): (a) deviator stress (kPa); (b) volumetric strain (%) (dilation shown as positive); (c) AE rate (RDC/min); (d) *b*-value; (e) AE generated per increment of boundary work (RDC/J)

ranging from 0·4 to 0·63, which confirms the influence of CN on AE generation. Relationships with stronger correlation would be expected with more accurate methods to quantify fabric (e.g. Hasan & Alshibli, 2010).

Unload–reload cycles

Figures 18 and 19 show results from load–unload–reload cycles on LBS 1·0–2·0 (test 16), which demonstrate that the Kaiser effect (Lavrov, 2003) occurs in particulate materials under cycles of both isotropic compression (Fig. 18) and

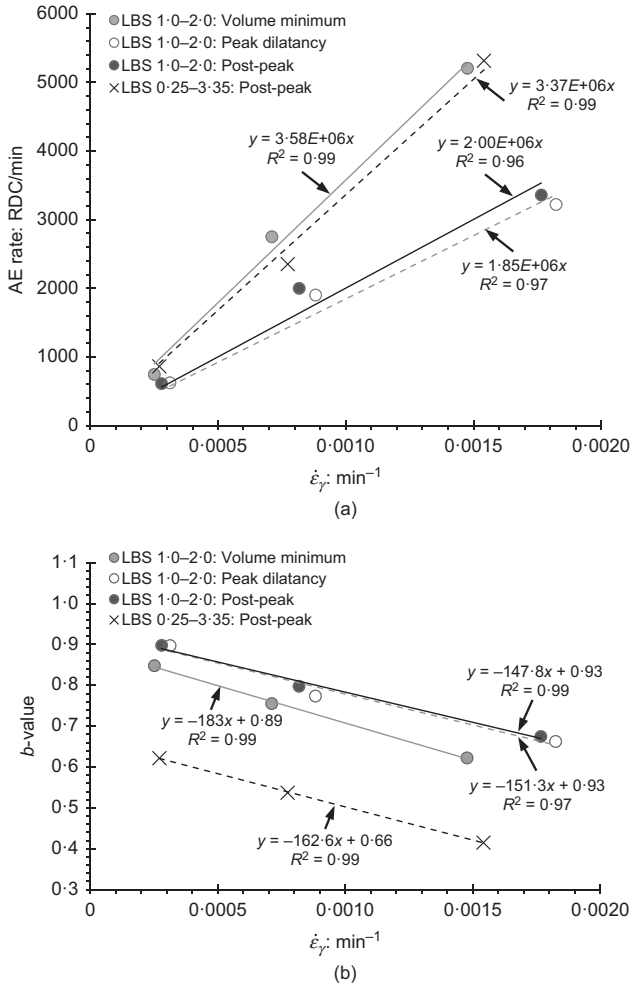

Fig. 13. (a) AE rate (RDC/min) and (b) *b*-value plotted against shear strain rate (per min) relationships (linear regressions) obtained from drained triaxial shearing tests at effective confining pressures of 300 kPa performed on LBS 1·0–2·0 and LBS 0·25–3·35 at axial displacement rates of 1, 3 and 6 mm/h (tests 9, 10, 11 and 15)

deviator stress (Fig. 19). Imposed unload and reload stages of isotropic compression were 50 kPa and 100 kPa, respectively. The unload cycles of deviator stress were initiated at approximately 35, 55 and 70% of peak shear strength. AE activity is negligible until the current stress conditions (compression and/or shear) exceed the maximum that the soil has been subjected to in the past.

DISCUSSION

A programme of drained triaxial tests have been performed on dense sands to establish quantified relationships for use in the interpretation of soil behaviour from AE measurements. The mechanical behaviour of the dense sands was consistent with findings reported in the literature: the obtained critical state friction angles of 33°±1° and dilatancy components ($\phi'_p - \phi'_{cv}$, Table 2) of 8° ± 1° are typical for quartz sands with an initial relative density of approximately 85% (Bolton, 1986); and the peak dilation rates and corresponding state parameters (e.g. Table 2 and Fig. 10(b)) fit within the range of experimental data reported for 29 sands (Been & Jefferies, 1986; Been *et al.*, 1991; Yang & Li, 2004).

The combination of *b*-value and AE rates has been measured from particulate materials for the first time in triaxial isotropic compression and shearing. The results show that AE generation in granular soils is proportional to the imposed stress level and strain rate, which agrees with previous findings (e.g. Koerner *et al.*, 1981; Tanimoto & Nakamura, 1981). Uniquely, their influence has been quantified in this study through a series of empirical relationships (Figs 6, 10 and 13).

Previous research has shown that particulate materials experience the Kaiser effect in compression (e.g. Koerner *et al.*, 1984; Dixon *et al.*, 1996) and this study has extended knowledge to demonstrate its existence in shearing: AE activity in particulate materials is negligible until the current stress conditions (compression and/or shear) exceed the maximum that has been experienced in the past, due to the Kaiser effect.

Tanimoto & Nakamura (1981) presented results from a limited number of triaxial shearing tests to show that the AE response increased linearly with strain until volume minimum, whereupon it then became constant. This study has shown that there are in fact two types of AE response at the transition from contractive to dilative behaviour: type-1 exhibits a peak in AE rate activity in addition to a trough in *b*-value activity that reduces as the peak shear strength is mobilised and then remains relatively constant, whereas type-2 exhibits a trough in *b*-value that is less pronounced and no peak in AE rates. Mean particle size appears to govern which AE behaviour type dense sands will experience; this is supported by the results from both uniformly graded and more well-graded LBS (e.g. Fig. 9), and preliminary experiments performed on glass beads by the authors show the same trends. However, further tests on a range of sands with different gradings are required to conclude what controls the AE behaviour type.

An original contribution of this study has been quantification of relationships between AE and boundary work (i.e. RDC generated per Joule) for a unit volume of sand under isotropic compression and shear (R^2 ranging from 0·58 to 0·98), which show that dense sands in shear generate greater RDC/J than they do in isotropic compression (e.g. approximately 10 000 RDC/J in isotropic compression, approximately 20 000–35 000 RDC/J in shear). The amount of AE generated per increment of boundary work has been shown to be proportional to the fabric coordination number, and hence is greatest at the transition from contractive to dilative behaviour and then reduces, becoming steady when shear strains localise into a concentrated, dilating shear zone with large void ratio. In addition, this study has produced new quantified relationships between AE rates, *b*-value and shear strain rate (R^2 ranging from 0·96 to 0·99), enabling interpretation of accelerating deformation behaviour that typically ensues following mobilisation of peak shear strength in a body of soil (e.g. quantification of increasing shear strain rates that occur in a stress-controlled system using the relationships shown in Fig. 13).

Combining measurement of AE rates and *b*-values enables interpretation of the strength and deformation behaviour of particulate materials, which will facilitate early warning of serviceability and ultimate limit state failures in the field and enhance the instrumentation of element and physical model tests in the laboratory. An example of the novel interpretation concept is presented in Fig. 20, which illustrates how the current AE rate multiplied by the change in *b*-value could be used to identify the transition from contractive to dilative behaviour (i.e. $q/p' = M$), mobilisation of peak shear strength and quantify subsequent accelerating deformation behaviour. Combining AE rates and *b*-value measurements in this way could be beneficial because the transition from contractive to dilative behaviour becomes distinctly evident and hence easier to detect. Stress history is also an important consideration in the development of interpretation

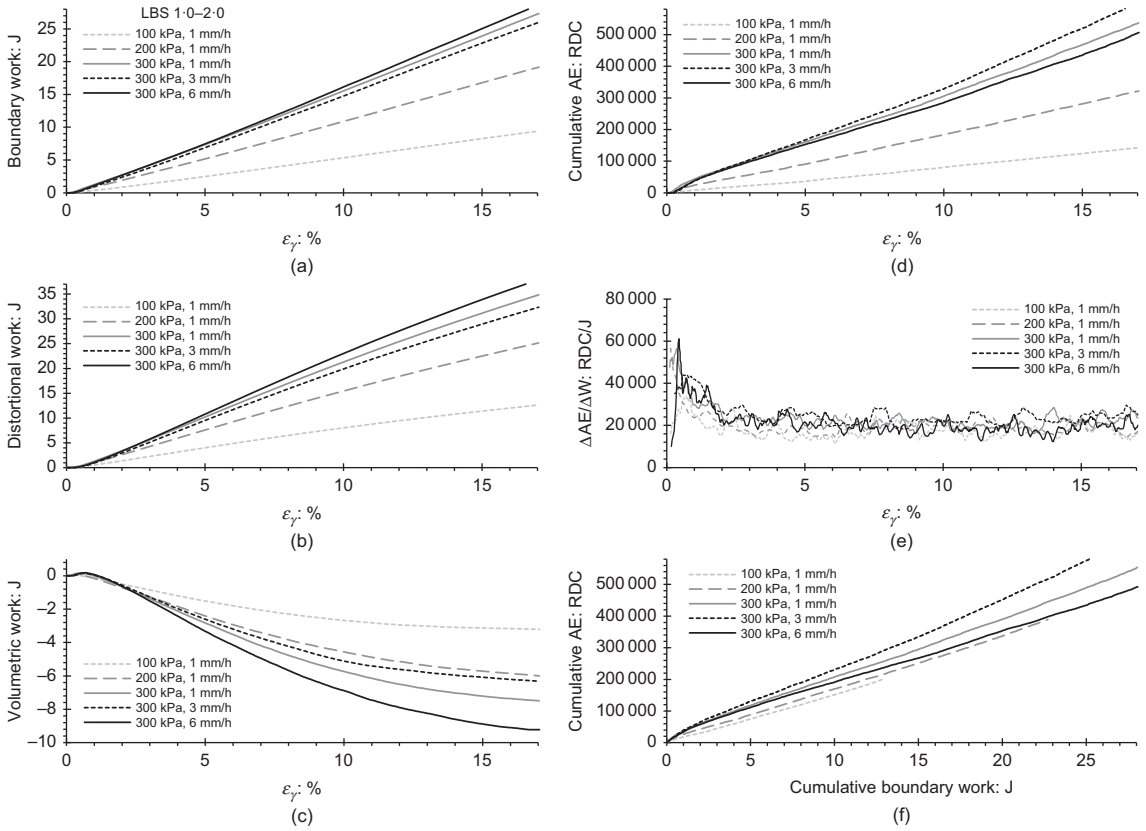

Fig. 14. Measurements plotted against shear strain (%) from drained triaxial shearing tests performed on LBS 1·0–2·0 (tests 7–11): (a) boundary work (J); (b) distortional work (J); (c) volumetric work (J); (d) cumulative AE (RDC); (e) AE generated per increment of boundary work (RDC/J); (f) cumulative AE (RDC) plotted against cumulative boundary work (J) relationships

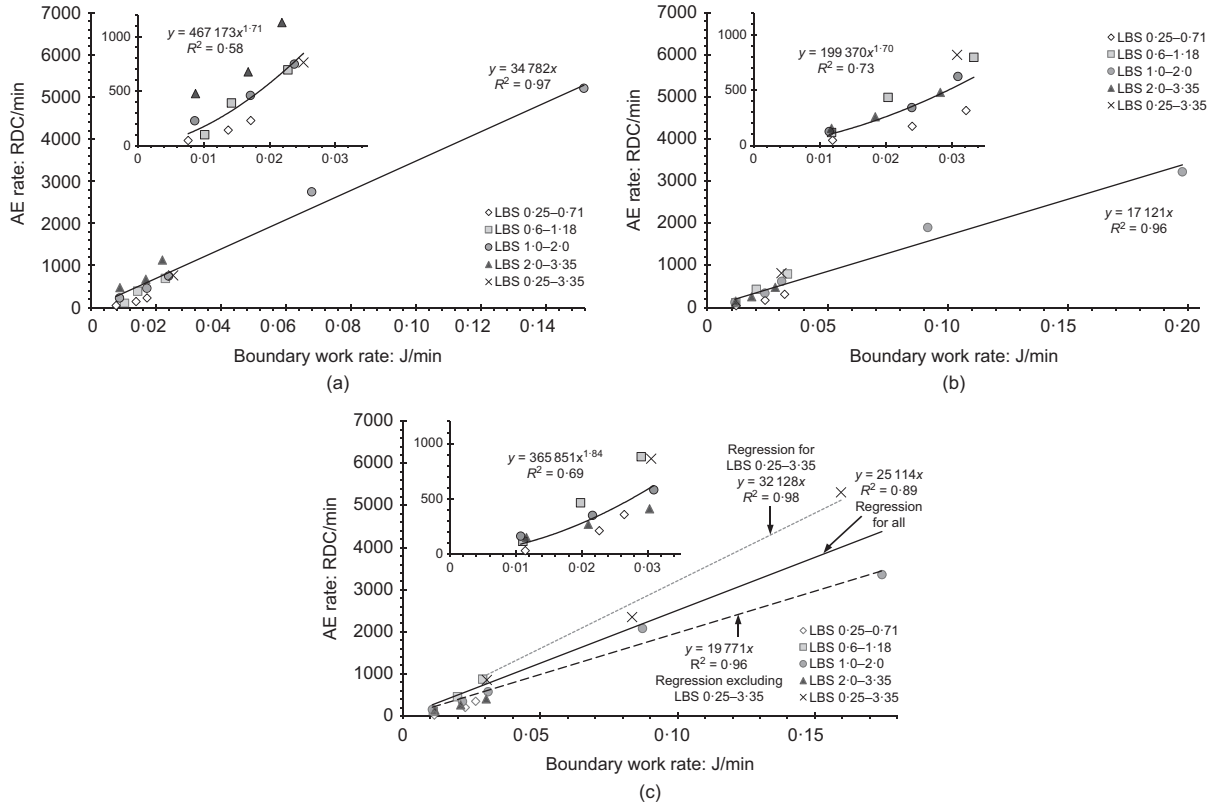

Fig. 15. Average AE rate (RDC/min) measurements plotted against average boundary work rate (J/min) measurements (tests 1–15) at: (a) volume minimum; (b) peak dilatancy; (c) post-peak

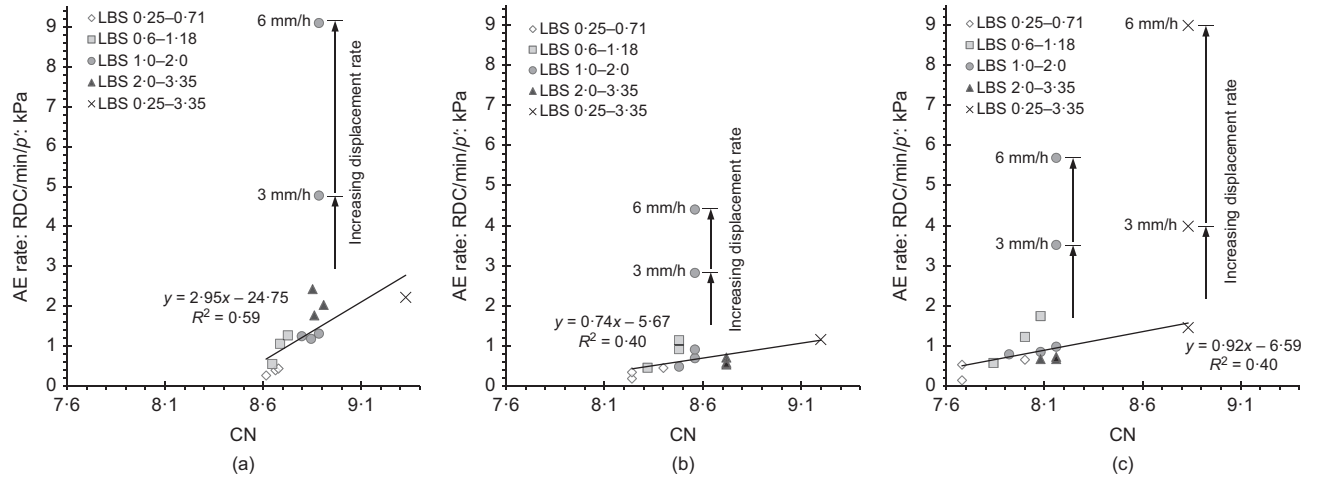

Fig. 16. Average AE rate (RDC/min) measurements normalised by the current mean effective stress plotted against coordination number (CN) (tests 1–15) at: (a) volume minimum; (b) peak dilatancy; (c) post-peak

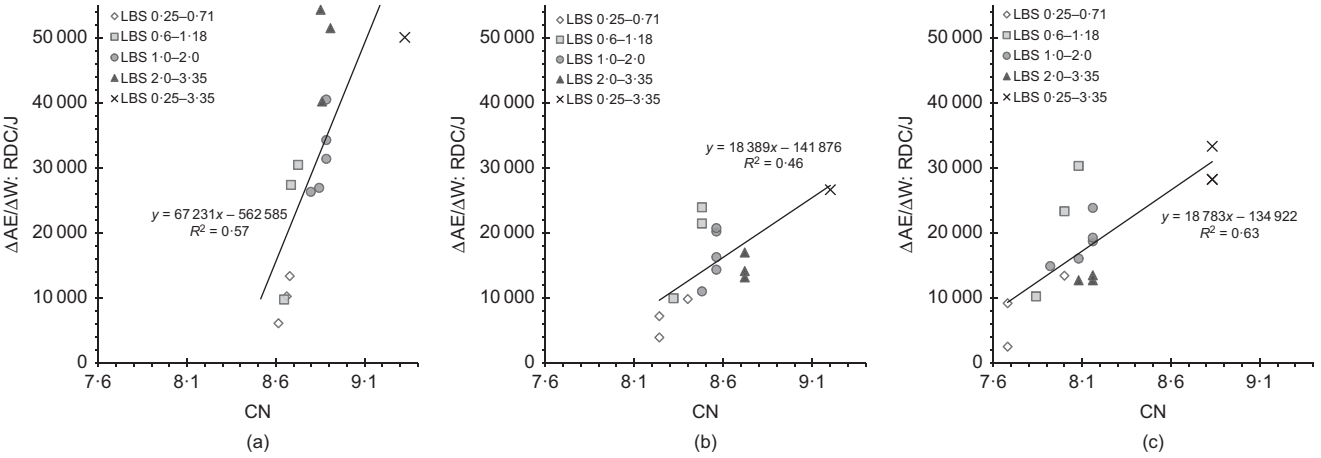

Fig. 17. Average AE generated per increment of boundary work (RDC/J) plotted against coordination number (CN) (tests 1–15) at: (a) volume minimum; (b) peak dilatancy; (c) post-peak

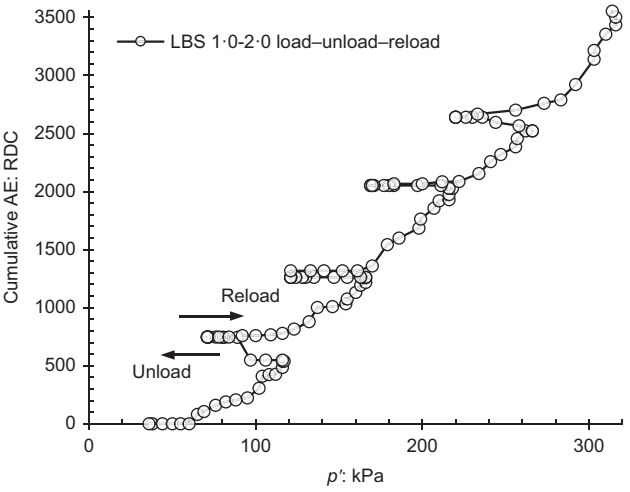

Fig. 18. Cumulative (AE) RDC plotted against mean effective stress (kPa) measurements for isotropic load–unload–reload cycles of cell pressure performed on LBS 1·0–2·0 (test 16)

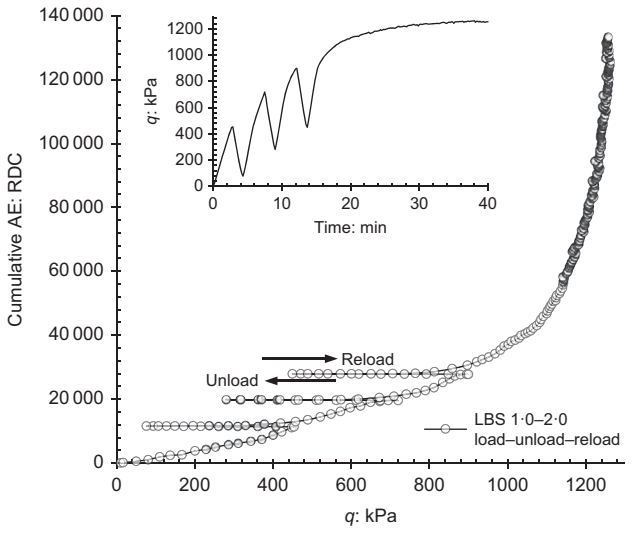

Fig. 19. Cumulative (AE) RDC plotted against deviator stress (kPa) measurements for load–unload–reload cycles of deviator stress (kPa) performed on LBS 1·0–2·0 at an effective confining pressure of 300 kPa and axial displacement rate of 6 mm/h. The inset shows deviator stress (kPa) plotted against time (test 16)

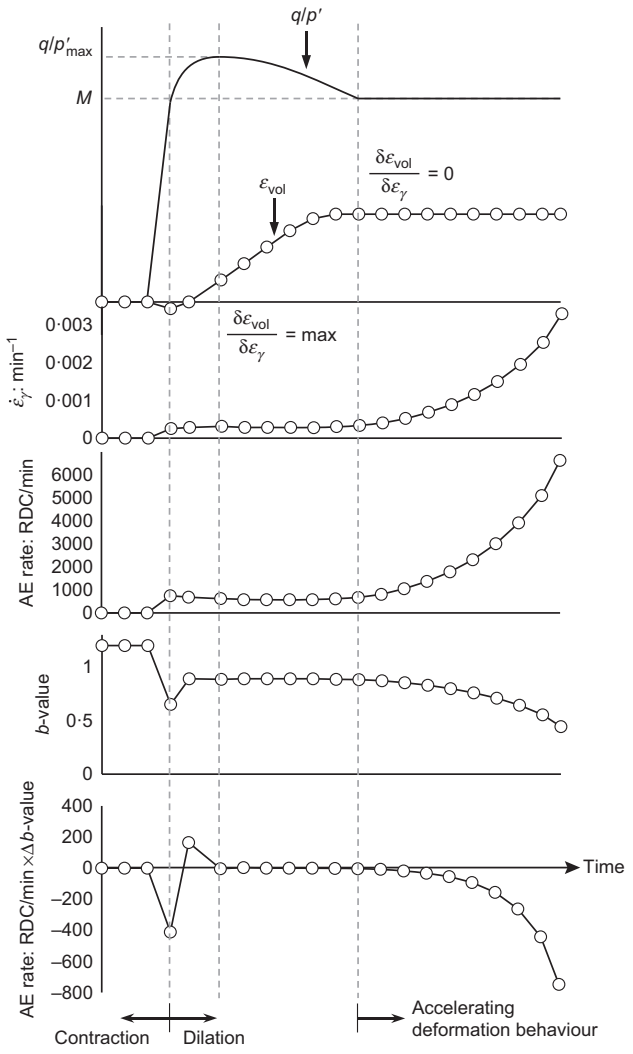

Fig. 20. Example use of AE for interpreting pre- and post-peak shear strength mobilisation and accelerating deformation behaviour. The example is based on measurements from LBS 1·0–2·0 at an effective confining pressure of 300 kPa and using the AE plotted against shear strain rate relationships in Fig. 13

methodologies: negligible AE could mean that the system is stable with no change to the stress state, or it could mean that the stress state has not reached the maximum that the system has been exposed to in the past.

The authors propose that future research into the AE behaviour of soils should progress in the following directions: (*a*) use of simple shear apparatus for greater control over the distribution of shear strains within specimens, which is more variable with conventional triaxial apparatus (i.e. variable failure modes between loose and dense specimens); (*b*) development of AE generation contact laws for discrete-element modelling, which will enable detailed investigation of fabric evolution and particle-scale interactions; and (*c*) use of artificial intelligence (e.g. deep learning) to develop automated interpretation of AE measurements.

CONCLUSIONS

This study has gone beyond the state-of-the-art and established quantitative interpretation of AE generated by particulate materials. This new knowledge will enable use of AE monitoring to provide early warning of serviceability and ultimate limit state failures in the field. It also demonstrates that innovative AE instrumentation and measurement can enhance insights into element and physical model tests in the laboratory. Results from a programme of drained triaxial tests on dense sands show the following points.

(*a*) AE rates generated by particulate materials are proportional to the imposed stress level, strain rate, fabric coordination number (estimated from an empirical relationship with void ratio in the research reported here) and the boundary work done.
(*b*) There are two types of AE response at the transition from contractive to dilative behaviour, which was governed by the mean particle size.
(*c*) AE activity in particulate materials is negligible until the current stress conditions (compression and/or shear) exceed the maximum that has been experienced in the past, due to the Kaiser effect.
(*d*) Relationships between AE and boundary work (i.e. RDC generated per Joule) have been quantified for a unit volume of sand under isotropic compression and shear, which show that dense sands in shear generate greater RDC/J than they do in isotropic compression.
(*e*) Relationships have also been quantified between AE rates, *b*-value and shear strain rate, enabling interpretation of accelerating deformation behaviour that typically ensues following mobilisation of peak shear strength in a body of soil.
(*f*) An example interpretation framework has been presented that combines AE rate and *b*-value measurements to identify the transition from contractive to dilative behaviour (i.e. $q/p' = M$), mobilisation of peak shear strength and quantify subsequent accelerating deformation behaviour that typically accompanies shear zone development.

ACKNOWLEDGEMENTS

The authors acknowledge the excellent technical assistance provided by Mr Lewis Darwin and the Loughborough Materials Characterisation Centre. Alister Smith gratefully acknowledges the support of an EPSRC Fellowship (Listening to Infrastructure, EP/P012493/1). Data reported in this study can be made available by the authors on request.

NOTATION

A	AE waveform amplitude
B	Skempton's pore pressure parameter
b-value	measure of the proportion of low and high magnitude events in an AE waveform
C_c	coefficient of curvature
C_u	coefficient of uniformity
D_r	relative density (%)
e_{max}	maximum void ratio
e_{min}	minimum void ratio
M	frictional constant defining the slope of the critical state line in q–p' space ($6\sin\phi'_{crit}/3 - \sin\phi'_{crit}$)
m	log-scale measure of AE magnitude
p'	mean effective stress (kPa)
q	deviator stress (kPa)
R_a	roughness average, the arithmetic average of the absolute values of the profile heights over the evaluation length (μm)
R_q	root-mean-square roughness, the root mean square average of the profile heights over the evaluation length (μm)
R_z	average maximum height of the profile, the average of the successive values of the vertical distance between the highest and lowest points of the profile within a sampling length calculated over the evaluation length (μm)

ΔW increment of work done per unit volume transmitted to the soil skeleton across its boundaries (i.e. boundary work)
ΔW_d increment of distortional work per unit volume
ΔW_v increment of volumetric work per unit volume
ε_a axial strain
ε_q deviatoric strain ($(2/3)\varepsilon_\gamma = (2/3)(\varepsilon_a - \varepsilon_r) = \varepsilon_a - (1/3)\varepsilon_{vol}$)
ε_r radial strain
ε_{vol} volumetric strain
ε_γ shear strain ($\varepsilon_a - \varepsilon_r = (1/2)(3\varepsilon_a - \varepsilon_{vol})$)
$\dot{\varepsilon}_\gamma$ shear strain rate (min^{-1})
$\rho_{dry_{max}}$ maximum dry density (Mg/m^3)
$\rho_{dry_{min}}$ minimum dry density (Mg/m^3)
ρ_s particle density (Mg/m^3)
σ'_r radial effective stress (kPa)
ϕ_μ inter-particle friction angle
ϕ'_{cv} constant volume friction angle
ϕ'_p peak effective friction angle
ψ state parameter

REFERENCES

Arthur, J. R. F. & Menzies, B. (1972). Inherent anisotropy in a sand. *Géotechnique* **22**, No. 1, 115–128, https://doi.org/10.1680/geot.1972.22.1.115.

Been, K. & Jefferies, M. G. (1985). A state parameter for sands. *Géotechnique* **35**, No. 2, 99–112, https://doi.org/10.1680/geot.1985.35.2.99.

Been, K. & Jefferies, M. G. (1986). Discussion: a state parameter for sands. *Géotechnique* **36**, No. 1, 123–132, https://doi.org/10.1680/geot.1986.36.1.123.

Been, K., Jefferies, M. G. & Hachey, J. (1991). Critical state of sands. *Géotechnique* **41**, No. 3, 365–381, https://doi.org/10.1680/geot.1991.41.3.365.

Berg, N., Smith, A., Russell, S., Dixon, N., Proudfoot, D. & Take, W. A. (2018). Correlation of acoustic emissions with patterns of movement in an extremely slow moving landslide at Peace River, Alberta, Canada. *Can. Geotech. J.* **55**, No. 10, 1475–1488, https://doi.org/10.1139/cgj-2016-0668.

Bishop, A. W. & Wesley, L. D. (1975). A hydraulic triaxial apparatus for controlled stress path testing. *Géotechnique* **25**, No. 4, 657–670, https://doi.org/10.1680/geot.1975.25.4.657.

Bolton, M. D. (1986). The strength and dilatancy of sands. *Géotechnique* **36**, No. 1, 65–78, https://doi.org/10.1680/geot.1986.36.1.65.

Bolton, M. D. (2003). *A guide to soil mechanics*. London, UK: Universities Press.

BSI (2016). BS EN ISO 17892: Geotechnical investigation and testing – laboratory testing of soil. London, UK: BSI.

Cavarretta, I., Coop, M. & O'Sullivan, C. (2010). The influence of particle characteristics on the behaviour of coarse grained soils. *Géotechnique* **60**, No. 6, 413–423, https://doi.org/10.1680/geot.2010.60.6.413.

Cavarretta, I., Rocchi, I. & Coop, M. R. (2011). A new interparticle friction apparatus for granular materials. *Can. Geotech. J.* **48**, No. 12, 1829–1840.

Chang, C. S., Misra, A. & Sundaram, S. S. (1990). Micromechanical modelling of cemented sands under low amplitude oscillations. *Géotechnique* **40**, No. 2, 251–263, https://doi.org/10.1680/geot.1990.40.2.251.

Cho, G. C., Dodds, J. & Santamarina, J. C. (2006). Particle shape effects on packing density, stiffness, and strength: natural and crushed sands. *J. Geotech. Geoenviron. Engng* **132**, No. 5, 591–602.

Cui, L. & O'Sullivan, C. (2006). Exploring the macro- and micro-scale response of an idealised granular material in the direct shear apparatus. *Géotechnique* **56**, No. 7, 455–468, https://doi.org/10.1680/geot.2006.56.7.455.

Cui, L., O'Sullivan, C. & O'Neill, S. (2007). An analysis of the triaxial apparatus using a mixed boundary three-dimensional discrete element model. *Géotechnique* **57**, No. 10, 831–844, https://doi.org/10.1680/geot.2007.57.10.831.

Cundall, P. A. & Strack, O. D. (1979). A discrete numerical model for granular assemblies. *Géotechnique* **29**, No. 1, 47–65, https://doi.org/10.1680/geot.1979.29.1.47.

Desrues, J., Chambon, R., Mokni, M. & Mazerolle, F. (1996). Void ratio evolution inside shear bands in triaxial sand specimens studied by computed tomography. *Géotechnique* **46**, No. 3, 529–546, https://doi.org/10.1680/geot.1996.46.3.529.

Dixon, N., Kavanagh, J. & Hill, R. (1996). Monitoring landslide activity and hazard by acoustic emission. *J. Geol. Soc. China* **39**, No. 4, 437–464.

Dixon, N., Spriggs, M. P., Smith, A., Meldrum, P. & Haslam, E. (2015a). Quantification of reactivated landslide behaviour using acoustic emission monitoring. *Landslides* **12**, No. 3, 549–560.

Dixon, N., Smith, A., Spriggs, M., Ridley, A., Meldrum, P. & Haslam, E. (2015b). Stability monitoring of a rail slope using acoustic emission. *Proc. Instn Civ. Engrs – Geotech. Engng* **168**, No. 5, 373–384, https://doi.org/10.1680/jgeen.14.00152.

Dixon, N., Smith, A., Flint, J. A., Khanna, R., Clark, B. & Andjelkovic, M. (2018). An acoustic emission landslide early warning system for communities in low-income and middle-income countries. *Landslides* **15**, No. 8, 1631–1644, https://doi.org/10.1007/s10346-018-0977-1.

Garga, V. K. & Chichibu, A. (1990). A study of AE parameters and shear strength of sand. *Progress in acoustic emission V 10th acoustic emission symposium*, Sendai, Japan, vol. 5, pp. 129–136.

Hanley, K. J., Huang, X. & O'Sullivan, C. (2017). Energy dissipation in soil samples during drained triaxial shearing. *Géotechnique* **68**, No. 5, 421–433, https://doi.org/10.1680/jgeot.16.P.317.

Hasan, A. & Alshibli, K. A. (2010). Experimental assessment of 3D particle-to-particle interaction within sheared sand using synchrotron microtomography. *Géotechnique* **60**, No. 5, 369–379, https://doi.org/10.1680/geot.2010.60.5.369.

Head, K. H. (1986). *Manual of laboratory testing, volume 3: effective stress tests*. London, UK: ELE International Ltd.

Ibraim, E., Luo, S. & Diambra, A. (2017). Particle soil crushing: passive detection and interpretation. In *Proceedings of the 19th international conference on soil mechanics and geotechnical engineering* (eds W. Lee, J.-S. Lee, H.-K. Kim and D.-S. Kim), pp. 389–392. London, UK: International Society for Soil Mechanics and Geotechnical Engineering.

Koerner, R. M., Lord, A. E. Jr., Mccabe, W. M. & Curran, J. W. (1976). Acoustic emission behavior of granular soils. *J. Geotech. Geoenviron. Engng* **102**, No. 7, 761–773.

Koerner, R. M., Lord, A. E. Jr. & McCabe, W. M. (1978). Acoustic emission monitoring of soil stability. *J. Geotech. Geoenviron. Engng* **104**, No. 5, 571–582.

Koerner, R. M., McCabe, W. M. & Lord, A. E. (1981). Acoustic emission behavior and monitoring of soils. In *Acoustic emissions in geotechnical engineering practice* (eds V. P. Drnevich and R. E. Gray), ASTM STP 750, pp. 93–141. West Conshohocken, PA, USA: ASTM International.

Koerner, R. M., Lord, A. E. Jr & Deutsch, W. L. (1984). Determination of prestress in granular soils using AE. *J. Geotech. Engng* **110**, No. 3, 346–358.

Krumbein, W. C. & Sloss, L. L. (1963). *Stratigraphy and sedimentation*, 2nd edn. San Francisco, CA, USA: Freeman and Company.

Lavrov, A. (2003). The Kaiser effect in rocks: principles and stress estimation techniques. *Int. J. Rock Mech. Min. Sci.* **40**, No. 2, 151–171.

Lin, W., Mao, W., Koseki, J. & Liu, A. (2018). Frequency response of acoustic emission to characterize particle dislocations in sandy soil. In *Proceedings of GeoShanghai international conference: fundamentals of soil behaviours* (eds A. Zhou, J. Tao, X. Gu and L. Hu), pp. 689–697. Singapore: Springer.

López-Querol, S. & Coop, M. R. (2012). Drained cyclic behaviour of loose Dogs Bay sand. *Géotechnique* **62**, No. 4, 281–289, https://doi.org/10.1680/geot.8.P.105.

Mao, W. & Towhata, I. (2015). Monitoring of single-particle fragmentation process under static loading using acoustic emission. *Appl. Acoust.* **94**, 39–45.

Mao, W., Aoyama, S., Goto, S. & Towhata, I. (2015). Acoustic emission characteristics of subsoil subjected to vertical pile loading in sand. *J. Appl. Geophys.* **119**, 119–127.

Mao, W., Aoyama, S., Goto, S. & Towhata, I. (2016). Behaviour and frequency characteristics of acoustic emissions from sandy ground under model pile penetration. *Near Surf. Geophys.* **14**, No. 6, 515–525.

Mao, W., Aoyama, S. & Towhata, I. (2018a). Feasibility study of using acoustic emission signals for investigation of pile

spacing effect on group pile behaviour. *Appl. Acoust.* **139**, 189–202.
Mao, W., Yang, Y., Lin, W., Aoyama, S. & Towhata, I. (2018b). High frequency acoustic emissions observed during model pile penetration in sand and implications for particle breakage behavior. *Int. J. Geomech.* **18**, No. 11, 04018143.
Michlmayr, G. & Or, D. (2014). Mechanisms for acoustic emissions generation during granular shearing. *Granular Matter* **16**, No. 5, 627–640.
Michlmayr, G., Cohen, D. & Or, D. (2013). Shear-induced force fluctuations and acoustic emissions in granular material. *J. Geophys. Res.: Solid Earth* **118**, No. 12, 6086–6098.
Michlmayr, G., Chalari, A., Clarke, A. & Or, D. (2017). Fiber-optic high-resolution acoustic emission (AE) monitoring of slope failure. *Landslides* **14**, No. 3, 1139–1146.
Mirghasemi, A. A., Rothenburg, L. & Matyas, E. L. (2002). Influence of particle shape on engineering properties of assemblies of two-dimensional polygon-shaped particles. *Géotechnique* **52**, No. 3, 209–217, https://doi.org/10.1680/geot.2002.52.3.209.
Mitchell, R. J. & Romeril, P. M. (1984). Acoustic emission distress monitoring in sensitive clay. *Can. Geotech. J.* **21**, No. 1, 176–180.
Muir Wood, D. (1990). *Soil behaviour and critical state soil mechanics*. Cambridge, UK: Cambridge University Press.
Naderi-Boldaji, M., Bahrami, M., Keller, T. & Or, D. (2017). Characteristics of acoustic emissions from soil subjected to confined uniaxial compression. *Vadose Zone J.*, https://doi.org/10.2136/vzj2017.02.0049.
Oda, M. (1972). Initial fabrics and their relations to mechanical properties of granular material. *Soils Found.* **12**, No. 1, 17–36.
Oda, M. (1977). Co-ordination number and its relation to shear strength of granular material. *Soils Found.* **17**, No. 2, 29–42.
Pollock, A. A. (1973). Acoustic emission-2: acoustic emission amplitudes. *Non-Destructive Testing* **6**, No. 5, 264–269.
Powrie, W. (2013). *Soil mechanics: concepts and applications*. Boca Raton, FL, USA: CRC Press.
Sadrekarimi, A. & Olson, S. M. (2011). Critical state friction angle of sands. *Géotechnique* **61**, No. 9, 771–783, https://doi.org/10.1680/geot.9.P.090.
Senetakis, K., Coop, M. R. & Todisco, M. C. (2013). The inter-particle coefficient of friction at the contacts of Leighton Buzzard sand quartz minerals. *Soils Found.* **53**, No. 5, 746–755.
Shiotani, T. & Ohtsu, M. (1999). Prediction of slope failure based on AE activity. In *Acoustic emission: standards and technology update* (ed. S. J. Vahaviolos), pp. 156–172. West Conshohocken, PA, USA: ASTM International.
Skempton, A. W. (1954). The pore-pressure coefficients A and B. *Géotechnique* **4**, No. 4, 143–147, https://doi.org/10.1680/geot.1954.4.4.143
Smith, A. & Dixon, N. (2015). Quantification of landslide velocity from active waveguide–generated acoustic emission. *Can. Geotech. J.* **52**, No. 4, 413–425.
Smith, A., Dixon, N., Meldrum, P., Haslam, E. & Chambers, J. (2014). Acoustic emission monitoring of a soil slope: comparisons with continuous deformation measurements. *Géotechnique Lett.* **4**, No. 4, 255–261, https://doi.org/10.1680/geolett.14.00053.
Smith, A., Dixon, N. & Fowmes, G. (2017). Early detection of first-time slope failures using acoustic emission measurements: large-scale physical modelling. *Géotechnique* **67**, No. 2, 138–152, https://doi.org/10.1680/jgeot.15.P.200.
Tanimoto, K. & Nakamura, J. (1981). Studies of acoustic emission in soils. In *Acoustic emissions in geotechnical engineering practice* (eds V. P. Drnevich and R. E. Gray), ASTM STP 750, pp. 164–173. West Conshohocken, PA, USA: ASTM International.
Tanimoto, K. & Tanaka, Y. (1986). Yielding of soil as determined by acoustic emission. *Soils Found.* **26**, No. 3, 69–80.
Wan, R. G. & Guo, P. J. (2004). Stress dilatancy and fabric dependencies on sand behavior. *J. Engng Mech.* **130**, No. 6, 635–645.
Yang, J. & Li, X. S. (2004). State-dependent strength of sands from the perspective of unified modeling. *J. Geotech. Geoenviron. Engng* **130**, No. 2, 186–198.
Zheng, J. & Hryciw, R. D. (2015). Traditional soil particle sphericity, roundness and surface roughness by computational geometry. *Géotechnique* **65**, No. 6, 494–506, https://doi.org/10.1680/geot.14.P.192.